Optimization of Transcutaneous Energy Transfer Coils for High Power Medical Applications

O. Knecht,
R. Bosshard,
J. W. Kolar,
C. T. Starck

Optimization of Transcutaneous Energy Transfer Coils for High Power Medical Applications

O. Knecht*, R. Bosshard*, J. W. Kolar*, and C. T. Starck†

*Power Electronic Systems Laboratory, ETH Zürich, Switzerland, Email: knecht@lem.ee.ethz.ch
†Division of Cardiovascular Surgery, University Hospital Zurich, Switzerland

Abstract—Inductive Power Transfer (IPT) technology is a promising solution for powering medical implants with a continuous high power consumption, due to the elimination of the percutaneous driveline, which is still the major cause of severe infections. However, at the present time, no Transcutaneous Energy Transfer (TET) system is commercially available and ready for long-term use. Specifically the heating of the tissue due to power losses in the TET coils is a major problem. The focus of this paper therefore is on the minimization of the power losses in the energy transmission and receiver coils of a TET system. Extensive parameter sweeps were performed in order to find the optimal winding configuration with minimized parasitic resistances and optimal inductance value. A thermal model of the human skin is developed to estimate the thermal limits. Based on the results, a prototype TET system is built to validate the optimization process. The prototype system is capable of transmitting 30 W of power with an efficiency greater than 93 %, even at a coil separation distance of 20 mm (0.79 in) and 70 mm (2.76 in) coil diameter.

Index Terms—Transcutaneous Energy Transfer, Inductive Power Transfer, Resonant Converter, Thermal Modeling

I. INTRODUCTION

In the industrial nations, an ever-growing number of people suffer from severe heart failure. At the end stage, a heart transplantation is the only curative treatment. However, the availability of suitable donor hearts is very limited. This trend promotes the development of Mechanical Circulatory Support Systems (MCSS), such as Left Ventricular Assist Devices (LVADs). Recent progress in the development of continuous flow LVADs, which are smaller in volume and of lower mechanical complexity than early developments, make a fully implantable solution the next logical step in the optimization of MCSS [1]. The idea of powering an artificial heart via an inductively coupled resonator originated in 1960 [2]. Nevertheless, in today's MCSS, the power supply is still connected to the blood pump via a percutaneous driveline, which is responsible for the majority of device related infections [3]. Even though Transcutaneous Energy Transfer (TET) systems have been successfully tested in a small number of patients [4], there are several unresolved problems and further technological improvements needed to enhance the reliability and safety of this technology.

In response to the limitations of existing technology, the Zurich Heart Project was founded in 2013 as a collaboration of the ETH Zurich, the University of Zurich and the University Hospital of Zurich, supported by Hochschulmedizin Zurich. The aim of the project is to develop new circulatory support devices and to optimize existing technology, including the development of a TET system and make improvements in particular with respect to reliability issues and robustness, as well as heat management. Hence, this paper describes the efficiency optimization/loss minimization of the energy transmission coils and the development of a prototype TET system.

In **Section II**, the concept of a fully implantable MCSS is introduced and the main challenges associated with the TET system are outlined. The optimization of the energy transmission coils requires good knowledge of the resonant converter they are operated in. Therefore, in **Section III** the electrical characteristics of the proposed converter topology are presented in detail and analyzed analytically. **Section IV** shows the optimization procedure of the energy transmission coils. In addition, to estimate the temperature of the tissue surrounding the receiver coil, a thermal model of the human skin is developed. In a next step, in order to validate the mathematical models and the theoretical analysis used in the optimization process, a prototype TET system is built and is presented with measurements in **Section V**. Finally, a discussion of the obtained results and future prospects are given in **Section VI**.

II. SYSTEM OVERVIEW AND DESIGN CHALLENGES

A fully implantable mechanical circulatory support system employs four key parts, which are the TET system, the control and communication electronics, the internal battery backup, and the blood pump itself. A detailed illustration of the system concept is given in **Fig. 1**. An external battery pack provides the main power supply to operate the LVAD. An inverter circuit as part of the TET system supplies the transmitter coil winding, which is placed in close proximity to the surface of the skin. The energy is transferred by electromagnetic induction to the receiver winding, which is implanted underneath the skin. On the secondary side, the induced AC voltage is rectified to a DC voltage and is applied to the motor inverter driving the LVAD.

An internal battery backup permits a fully untethered operation of the LVAD and facilitates activities that demand increased mobility of the patient. Today's implantable lithium-ion batteries provide energy densities of up to 255 Wh/l [5]. With a battery volume of about 8 cl and an average power consumption of approximately 7 W, the blood pump could be operated independently for 1-2 h, depending on the allowed depth of discharge. A charging controller supplies the internal lithium-ion battery and provides fast control of the battery voltage. Furthermore, a wireless communication channel is used to enable feedback control of the power transferred through the skin and to transmit monitoring data.

There are two main challenges associated with the operation of a TET system. First, the coupling of the two energy transmission coils is low and can vary greatly during operation, since the position of the coils can vary with movements of the patient. Additionally, the data transfer rate of the wireless communication is limited and there is the possibility of a failure within the communication channel itself. Nevertheless, a tight control of the TET system's output voltage is mandatory for a reliable operation of the implanted system. It is
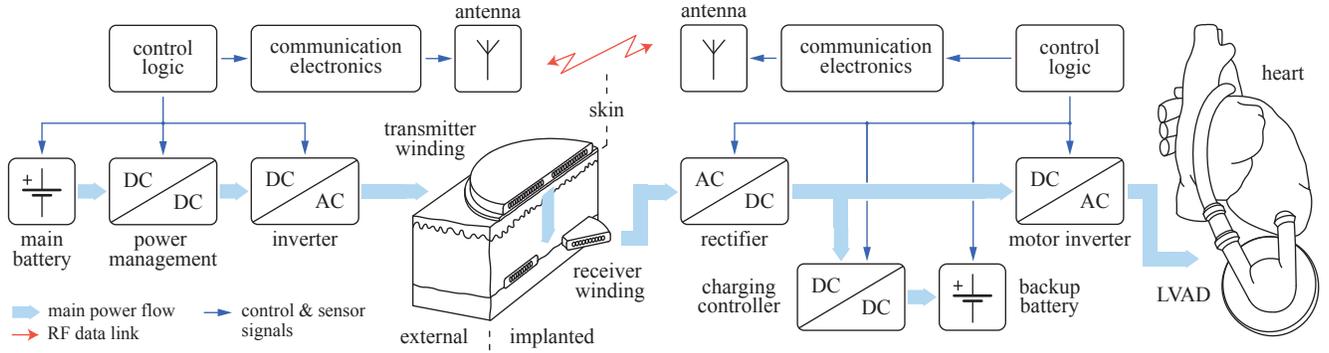
Figure 1: Schematic concept of an implantable mechanical circulatory support system (MCSS). The main power source is provided by an external battery pack, which is carried by the patient. An inverter circuit is used to feed the inductive power transfer coils. The electrical power is transmitted through the skin to an implanted receiver winding by induction. A rectifier circuit provides a DC voltage to the motor inverter that drives the LVAD. Additionally, a backup battery is implanted to enable untethered operation of the assist device. A wireless data link is incorporated to implement a closed-loop control of the TET system and the transmission of telemetry data.

therefore proposed to include an additional DC-DC converter before the implanted battery to relax the constraints on the control of the TET system and to protect the internal battery from unpredictable changes in the operating conditions.

Second, the power loss in the transmission system must be sufficiently low to keep the heat dissipation inside the body within save limits. The nominal power requirements for the TET system powering a LVAD is in the range of 8 to 12 W [1]. However, for the additional charging of the implanted battery and some added margin, a total power delivery of 25 to 30 W is required. Specifically in a full load condition, excessive heat generation can lead to permanent tissue damage. The minimization of the secondary side power loss is, therefore, one of the main objectives in the optimization process of the TET system, which is the focus of the subsequent sections.

III. IPT System Topology & Characteristics

The selection of the converter topology of the TET system has a major influence on the design of the energy transfer coils and it also determines the distribution of the power losses within the TET system. The main challenge in the design of TET systems is the low magnetic coupling of the energy transmission coils. In order to increase the efficiency, the inductive power transfer coils are operated in a resonant converter topology, including capacitors on the primary and secondary side for the compensation of the large stray inductance. In a preliminary step, four promising topologies, known from previous literature [6]–[11], the series-series (SS), series-parallel (SP) and the series-series-parallel (SSP) compensation as well as the series-series compensated topology operated at conditions for load independent unity voltage gain (SSU) were studied and compared, regarding their transfer characteristics and specifically regarding the secondary side power losses. The resonant converter topologies are shown in **Fig. 2 a)-c)**. The main disadvantage of the parallel compensated topologies is the constant power loss due the reactive power circulating within the resonant circuit even at light loading conditions. This is specifically undesired on the secondary side of the TET system due to the heating of the skin and since the TET system will often be operated in a partial load condition, where only the power for the blood pump has to be transferred. The series-series compensated systems in contrast, operated at constant output

voltage, exhibit a behaviour, where the secondary side resonant peak current is decreasing with decreasing output power at the same rate. It is therefore proposed to use a series-series compensated topology for the TET system, even though the receiver coil inductance is of larger value than it would be the case for a series-parallel compensated topology with the same voltage transfer ratio and matching of the secondary side inductor to the maximum load [11]. However, a reduction of the receiver coil size is only of partial advantage. A larger coil geometry allows for higher inductances and higher quality factors. As a result, the losses within the coils are reduced and spread over a larger surface, which simplifies the cooling. Additionally, higher coupling factors between primary and secondary side coil can be achieved with an increased tolerance to misalignment. According to cardiology specialists of the University Hospital of Zurich the maximum feasible coil diameter is about 70 mm (2.76 in), which is used as a geometric limitation in the coil optimization shown in **Section IV**.

The topology considered in this paper is shown in **Fig. 2 a)**. The series resonant primary side is supplied by a full-bridge inverter. On the secondary side, a full-wave rectifier is used to convert the AC voltage into a DC output voltage. The blood pump and the motor inverter are modeled as resistive load, which is connected in parallel with the output of the TET system and the charging controller of the backup battery. The charging controller consists of a buck-type converter with synchronous rectification in order to allow bidirectional power flow, and is used to step down the TET system output voltage to a nominal battery voltage of 14.4 V.

The voltage transfer characteristics and the phase of the input impedance of the series-series compensated system described in this paper are shown in **Fig. 3 a)** and **b)** with respect to frequency and for variable loading conditions and coupling factors. The peak gain resonance frequency of the system is at $f_r = f_0\sqrt{1-k_0}$ and is below the operating frequency f_0, which is known as operating point with load independent voltage gain and is explained in detail in [7], [8], [10]. In order to operate the system at this specific operating point, the compensation capacitors have to be chosen as

$$C_1 = \frac{1}{\omega_0^2 L_1(1-k_0)} \quad \text{and} \quad C_2 = \frac{1}{\omega_0^2 L_2(1-k_0)}, \quad (1)$$
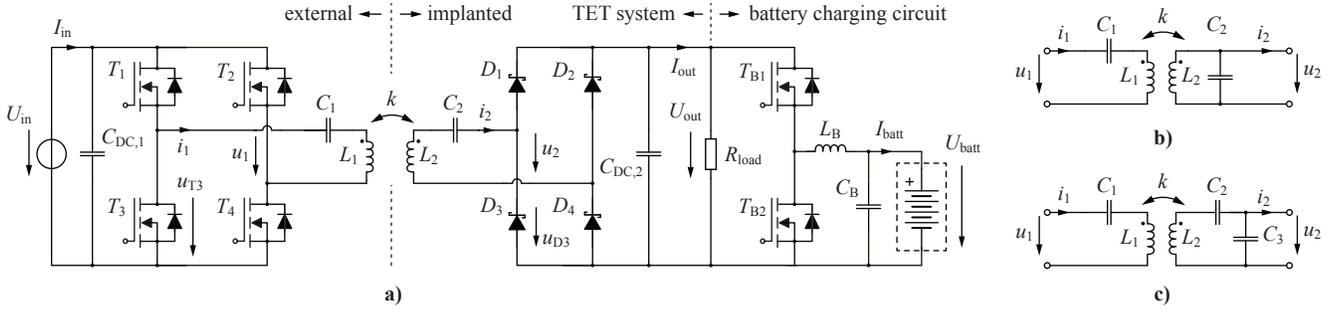
Figure 2: a) Proposed series-series resonant topology of the TET system and the backup battery charging controller. The motor inverter and the blood pump is modeled as a single equivalent load resistor. **b)-c)** show two other compensation methods for the resonant circuit.

where ω_0 is the angular operating frequency and L_1 and L_2 are the primary and secondary coil self-inductances respectively. The design variable k_0 is the coupling at which the system will exhibit a load independent voltage gain at the operating frequency f_0, and will be determined during the further design process. The actual coupling factor k can potentially have any value in the range of zero to one, independent of the parameter k_0.

Neglecting the parasitic resistances in the resonant system, the absolute value of the voltage transfer ratio at the operating frequency f_0 and at the coupling k_0 can be calculated as

$$|\underline{G}_v| = \left|\frac{\underline{u}_2}{\underline{u}_1}\right| = \sqrt{\frac{L_2}{L_1}} , \tag{2}$$

which is unity if the primary and secondary side coils are of equal inductance value, and is referred to as SSU operation. Note that with a fixed operating frequency f_0, the load independent voltage gain can only be achieved at the design coupling k_0. As the coupling k increases, the point of load independent voltage gain will move towards higher frequency.

It was shown in [11]–[13], that the energy transmission efficiency of an IPT system is maximal, if the load is matched to the secondary side inductance. Using a similar analysis, the transmission efficiency of the considered system at the operating frequency ω_0 can be calculated as

$$\eta_0 = \frac{\gamma_0 k^2 Q_1 Q_2^2}{1 + Q_2 \left(2\gamma_0 + k^2 Q_1 + \left(\gamma_0^2 + k_0^2 + \gamma_0 k^2 Q_1\right) Q_2\right)} , \tag{3}$$

where $\gamma_0 = \frac{R_{L,eq}}{\omega_0 L_2}$ denotes the load factor and Q_1 and Q_2 are the quality factors of the primary and secondary side coils respectively. According to [14], the equivalent load $R_{L,eq}$ is used to model the actual load together with the full-wave rectifier

$$R_{L,eq} = \frac{8}{\pi^2} \frac{U_{out}^2}{P_{out}} . \tag{4}$$

The efficiency of the resonant system is highest, if the load is matched to the secondary side coil described by the optimal load factor γ_{opt}

$$\gamma_{opt} = \frac{R_{L,eq}}{\omega_0 L_{2,opt}} = \frac{1}{Q_2}\sqrt{1 + k^2 Q_1 Q_2 + (k_0 Q_2)^2} . \tag{5}$$

If both, Q_1 and Q_2 are large (e.g. $Q > 200$), the optimal load factor can be approximated by

$$\gamma_{opt} \approx \sqrt{k^2 + k_0^2} . \tag{6}$$
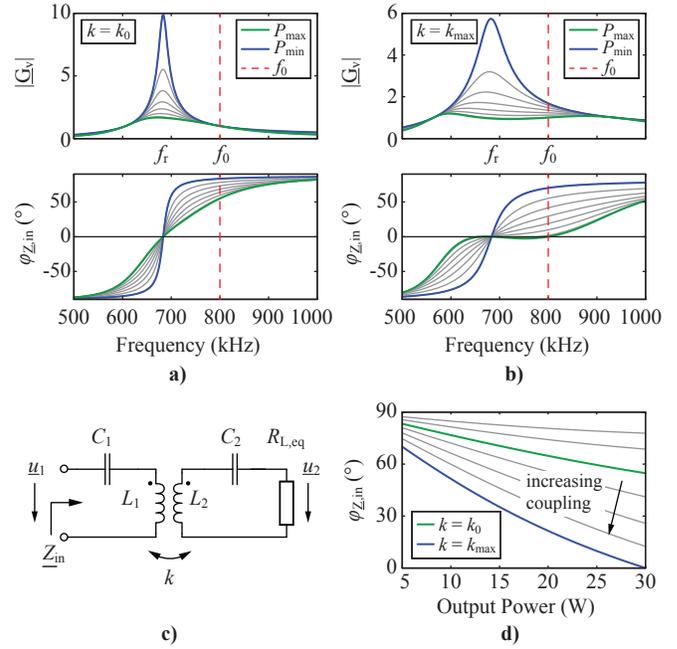
Figure 3: a)-b) Voltage transfer characteristics and phase angle of the input impedance of the considered series-series resonant energy transmission system, designed for an operation at 800 kHz, under variable loading conditions. **c)** Equivalent circuit of the resonant system used for the theoretical analysis. **d)** Phase angle of the input impedance at variable output power and coupling.

Using (4)-(6), at full load operation and at the coupling $k = k_0$, the optimal secondary side inductance can be found to be

$$L_{2,opt} = \frac{8}{\pi^2} \cdot \frac{U_{out}^2}{\sqrt{2}\omega_0 k_0 P_{out,max}} , \tag{7}$$

which is referred to as load matching condition.

Since the resonant circuit is supplied by a full-bridge inverter using Field Effect Transistors (FETs), which exhibit a finite output capacitance, the input impedance of the resonant network seen by the inverter has a great influence on the losses generated within the inverter itself. In order to achieve soft-switching, i.e. Zero Voltage Switching (ZVS) of the inverter switches, the input impedance of the resonant circuit must exhibit an inductive behaviour under all operating conditions. Using the equivalent circuit shown in **Fig. 3 c)**, the phase angle of the input impedance at the coupling k_0 and
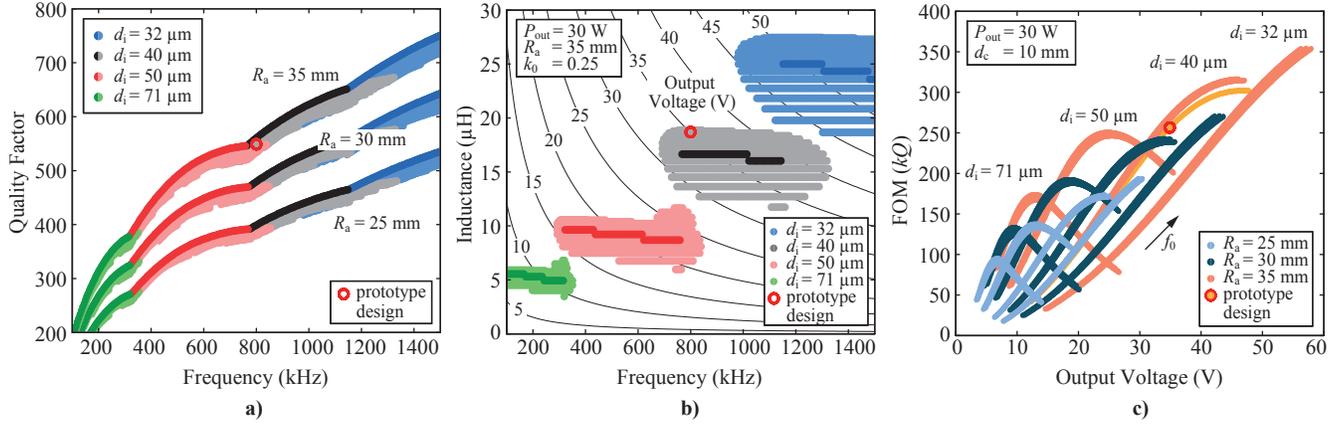
Figure 4: a) Designs with the maximum quality factor and designs that exhibit a high quality factor within 5 % of the maximum value for different coil diameters. **b)** Load matching plane defined by (7) for the same coil designs with an outside coil radius of 35 mm (1.38 in). **c)** Coil designs with the largest Figure-of-Merit $FOM = kQ$ at minimum coil separation distance with respect to the TET system output voltage.

operating frequency f_0 can be calculated as

$$\varphi_{\underline{Z},in} = \arccos\left(\frac{k_0 L_2 \omega_0}{\sqrt{R_{L,eq}^2 + k_0^2 L_2^2 \omega_0^2}}\right) \ . \tag{8}$$

Note that, under these operating conditions, the phase angle is independent of the primary side coil inductance L_1. If the maximum load is matched to the secondary side coil at the coupling $k = k_0$, the phase angle becomes

$$\varphi_{\underline{Z},in} = \arccos\left(\frac{1}{\sqrt{3}}\right) = 54.7° \ . \tag{9}$$

If the resonant system is designed for load matching at k_0, but during operation $k \neq k_0$, then the phase angle of the input impedance is equal to

$$\varphi_{Z,in} = \arccos\left(\sqrt{\frac{2}{3}} \frac{k^2}{\sqrt{k^4 - 2k^2 k_0^2 + 3k_0^4}}\right) \ . \tag{10}$$

The characteristic of the phase angle of the input impedance at the operating frequency f_0 is shown in **Fig. 3 d)**. The phase angle of the input impedance is decreasing with increasing coupling coefficient and increasing output power. In order to ensure that the phase angle is positive at maximum load, the system has to be designed for a coupling k_0 chosen as

$$k_0 \leq \frac{k_{max}}{\sqrt{3}} \ , \tag{11}$$

where k_{max} is the maximum achievable coupling with the system at hand. Given the coil geometry and the minimum spacing distance, k_{max} can be determined by experiment or simulation and the compensation capacitors can be designed using (1) and (11).

In order to validate the theoretical results shown in this section, the prototype system presented in **Section V** was designed such that the phase angle of the input impedance will be zero at maximum coupling and maximum output power. However, this means, that under this operating condition, soft-switching will be lost. Therefore, in a practical design, depending on the switches used in the inverter circuit, the coupling k_0 must be chosen lower, such that the phase angle of the input impedance is high enough and the remaining current provides sufficient charge to ensure soft-switching.
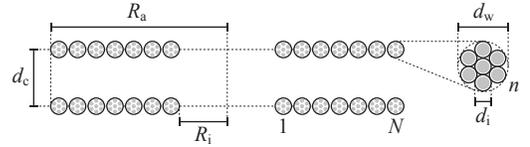
Figure 5: Schematic drawing of the cross section of the circular IPT coils including the geometry parameters of the parameter sweep. The geometry is defined by the inside and outside coil radius R_i and R_a, and the coil separation distance d_c. The litz-wire used for the windings has a diameter d_w and is composed of n strands with a diameter of d_i.

IV. COIL DESIGN AND OPTIMIZATION

For the coil design, it is proposed to use flat spiral coils with one layer of litz-wire winding to achieve a low profile and high mechanical flexibility. It was shown in previous publications that the theoretical maximal achievable efficiency of an IPT system is determined by the coupling factor and the quality factors of the inductors $\eta \approx 1 - 2/(k\sqrt{Q_1 Q_2})$ [12]. Therefore, the product kQ, with $Q = \sqrt{Q_1 Q_2}$ is the Figure-of-Merit *FOM* for the efficiency, which must be maximized to achieve a high energy transmission efficiency. The optimization process is based on the estimation of the coil losses and the coupling factor. Additionally, a thermal simulation model of the coils and the human skin was used to identify the feasible designs. The electrical operating conditions of the TET system are then found based on the estimation of the total secondary side power losses for the proposed topology shown in **Fig. 2**

A. Optimization Procedure

The coil optimization process was performed with parameter sweeps using both FE simulation and analytical models. It was shown in **Section III** that the primary and secondary side coils must have the same inductance value to achieve unity voltage gain at the matched loading. Therefore, the primary and secondary side coils are designed with equal winding configuration and geometry. The definitions of the coil geometry and the sweep parameters are shown in **Fig. 5**. The litz-wire was chosen from commercially available wires with strand diameters ranging from 32 to 71 μm (AWG 48 to 41) and number of strands ranging from 200 to 420. The outside coil radius was chosen between 25 and 35 mm (0.98 and 1.38 in).
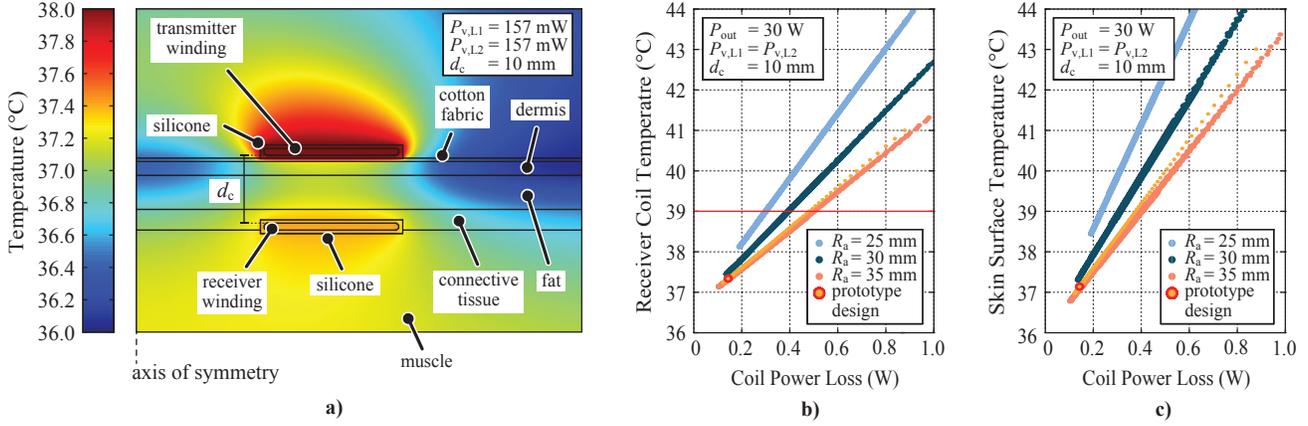
Figure 6: a) Structure of the two dimensional thermal model and the spatial temperature distribution of the prototype coils operated at the maximum output power and the minimum coil separation distance, where the primary and secondary side coil losses are equal. **b)-c)** Simulation results of the maximum surface temperature of the receiver coil and the skin for the coil designs found in **Section IV** under the same operating conditions.

The number of windings was increased subsequently for each type of litz wire, filling the given winding area up to a minimum inside coil radius of 4 mm. For the coil separation distance, a range of 10 to 25 mm (0.39 to 0.98 in) was specified in discussion with medical experts. Due to the large number (>10k combinations) of sweep parameters, the simulations are divided into three separate branches, which are computed in parallel to reduce the computation time. During the first simulation, the AC resistance and the self inductance value of each coil is computed. The AC losses of coils can be divided into DC, skin- and proximity-effect losses. With the considered strand diameters, the skin-effect losses can be reduced to the DC losses within the considered frequency range. Hence, only the proximity-effect losses contribute to the frequency dependent part of the total losses. In order to calculate the AC resistance of each coil design, the coils are simulated at a fixed frequency and the peak magnetic field is extracted in each conductor to calculate the proximity-effect losses. Given the field distribution and the peak current in each coil, the AC resistance can be extrapolated with good accuracy for the considered frequency range of 100 kHz to 1.5 MHz, using the analytical loss model for litz-wire windings described in [15]. Given the AC resistance and the self-inductance value, the quality factor can be calculated for each design for the specified frequency range. However, only the designs with the highest quality factor will be considered in the following steps of the optimization. **Fig. 4 a)** shows the designs with the maximum quality factor and all the designs which exhibit a high quality factor within a range of 5 % of the maximum value at each frequency. Additionally, the designs are coloured according to the corresponding litz-wire strand diameter.

In parallel, in the second simulation, the magnetic coupling between two equal coils was computed for all combinations of coil geometries and coil separation distances. Given the quality factor and the achievable coupling factors of each design, the optimal output voltage of the IPT system can be computed from (5). For a load matching at maximum power output and coupling k_0, the result is

$$U_{\text{out,opt}} = \frac{\left(2k_0^2 Q'^2 + 1\right)^{1/4} \cdot \pi \sqrt{2P_{\text{out,max}} \omega_0 L'}}{4\sqrt{Q'}}, \qquad (12)$$

where $L' = L_1 = L_2$ and $Q' = Q_1 = Q_2$ are used. With the approximation (6), this simplifies to

$$U_{\text{out,opt}} = \frac{2^{3/4}}{4} \pi \sqrt{k_0 \omega_0 L_2 P_{\text{out,max}}}. \qquad (13)$$

The load matching plane defined by (13) is shown in **Fig. 4 b)** for $k_0 = 0.25$ and $P_{\text{out}} = 30$W, and coil geometries with an outside radius of 35 mm (1.38 in). Only the designs with a high quality factor are highlighted, as it was done in **Fig. 4 a)**. The TET system output voltage that must be chosen to achieve load matching for a given coupling $k = k_0$ and output power P_{max} is indicated by the contour lines in the load matching plane. **Fig. 4 c)** shows the *FOM* of the same designs with respect to the optimal output voltage, calculated with (12), and designed for a coupling k_0, according to (11). The individual designs are colored according to the outside coil radius. As expected, the designs using the smallest strand diameter and the largest outside coil diameter have the highest *FOM*. It can also be seen, that for load matching at k_0, a higher *FOM* can be achieved with a higher output voltage.

B. Thermal Modeling of the IPT Coils

In order to estimate the maximum receiver coil and skin surface temperature, the third part of the simulation uses a general two dimensional thermal FE model of the skin structure and the embedded IPT coils as it is shown in **Fig. 6 a)**. The material properties of the living tissue are shown in **Tab. I**. In order to take the cooling capabilities of the living tissue and the metabolic heat sources into account, COMSOL's bioheat transfer module is used to model the heat transfer in the tissue, which is described by Penne's bioheat equation [17]. For the boundaries, a realistic worst case scenario was chosen, where it was assumed that the primary side coil is fully covered by textile fabric and thus, to some extent, thermally well isolated from the ambient, as it could be the case when the patient lies in a bed. To ensure proper electrical insulation, the coils are embedded in silicone. Additionally, the transmitter winding is separated from the bare skin by another layer of cotton fabric for thermal insulation. It was found in [17] that a continuous tissue temperature above 42°C will cause permanent tissue damage. Hence, a maximum value of 39°C was chosen as thermal limit for the secondary side coil surface

Table I: Thermal properties of the human skin and the layers of subcutaneous tissue used in the thermal model [16].

Material	Density $\left(\frac{kg}{m^3}\right)$	Thermal conductivity $\left(\frac{W}{m \cdot K}\right)$	Heat capacity $\left(\frac{J}{kg \cdot K}\right)$	Blood perfusion rate $\left(\frac{1}{s}\right)$	Metabolic heat source $\left(\frac{W}{m^3}\right)$
Dermis	1109	0.37	3391	0.00196	1829.8
Fat	911	0.21	2348	0.0005	464.6
Connective tissue	1027	0.39	2372	0.000634	595.7
Muscle	1090	0.49	3421	0.00071	1046.4
Blood	1050	0.52	3617	-	0

temperature to allow a margin for the temperature rise within the TET system. Following the design equations from **Section III**, it can be shown that at the minimum coil separation distance and at full overlap, the primary and secondary side coil currents have the same amplitude at maximum power throughput and experience therefore the same amount of power loss. The thermal simulations are performed to extract the maximum secondary side coil and the skin surface temperatures for the designs with highest quality factors found in the coil optimization process. The results are shown in **Fig. 6 a)** and **b)**. Depending on the outside coil radius, a power loss of up to 500 mW for the largest geometry and approximately 300 mW for the smallest coil design is allowed, in order to keep the tissue temperature below the specified limit. The spatial temperature distribution within the tissue and the selected prototype coils, with the specifications given in **Tab. II** and operated at full load and a coil separation distance of 10 mm (0.39 in) is shown in **Fig. 6 a)**. According to the simulation, the estimated secondary side coil surface temperature is well below the specified limit of 39°C.

C. Total Secondary Side Power Losses

In order to find the optimal coil design and electrical operation conditions, the total secondary side losses are calculated for each coil design with maximum *FOM*, excluding designs that violate the thermal constraints on the receiver coil temperature. The calculations include the losses in the receiver coil, the diode rectifier and the losses generated within the battery charging controller. For this purpose, a detailed mathematical loss model of the synchronous buck converter was created, including the switching losses of the gallium nitride FETs (EPC2016), which are used in the inverter circuit of the prototype system as well. The result of the calculations are shown in **Fig. 7**. The designs are shown for the optimal TET system output voltage as a function of the total secondary side power losses, colored according to the inverter's operating frequency. 1) shows the total secondary side losses excluding the battery charging controller, while 2) - 4) show the total secondray side losses including the buck-type charging controller operated at a switching frequency of 500 kHz, 1.5 MHz and 2.5 MHz, respectively. The volume occupation and the heating of the tissue due to the rectifier and charging controller are not considered in this analysis and will be the topic of future work. With the designs shown in 1), where the backup battery would be connected directly to the TET system's output, a total secondary side power loss of approximately 2 W will be generated for 14.4 V battery voltage. An even lower secondary side power loss could be achieved, if the TET system is operated at 800 kHz and an output voltage of 35 V, including the battery charging controller operated at a switching frequency of 500 kHz. This shows that including the buck converter, it
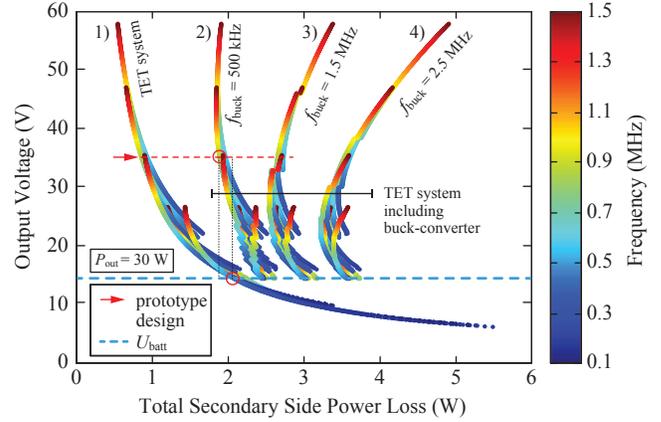
Figure 7: Optimal TET output voltage for the coil designs with highest *FOM* with respect to the total secondary side power losses, excluding designs that violate the thermal limit on the receiver coil temperature. The trajectories in 1) do not include the battery charging controller and describes only the secondary side power losses of the TET system. 2)-4) show the losses including the battery charging controller, operated at a switching frequency of 500 kHz, 1.5 MHz and 2.5 MHz. The designs are colored according to the switching frequency of the primary side inverter circuit.

is possible to use coil designs with a much higher *FOM*, than it would be the case at a TET system output voltage of 14.4 V and, hence, achieving lower losses within the TET system. The corresponding coil design was built and is described in detail in **Section V**.

V. EXPERIMENTAL VERIFICATION

In order to validate the theoretical considerations of the SSU system operation and the results obtained from the optimization process, a converter board and the selected prototype coils were realized in hardware. In the following, the specifications and the structure of the prototype TET system are given, along with measurements of the performance and the electrical characteristics.

A. Prototype TET System

Fig. 8 a) and **b)** show a photograph of the converter board and the TET system assembly including the prototype coils. The specifications of the prototype coils and the driving circuit are given in **Tab. II a)** and **b)**. The prototype coils have an outside diameter of 70 mm (2.76 in) and are wound with 16 turns of litz-wire on a single layer. Due to reasons of availability, the litz-wire consist of 300 strands instead of the wire used in the optimization with 320 strands.

The prototype system includes the primary and secondary side circuit of the TET system without the battery charging controller.
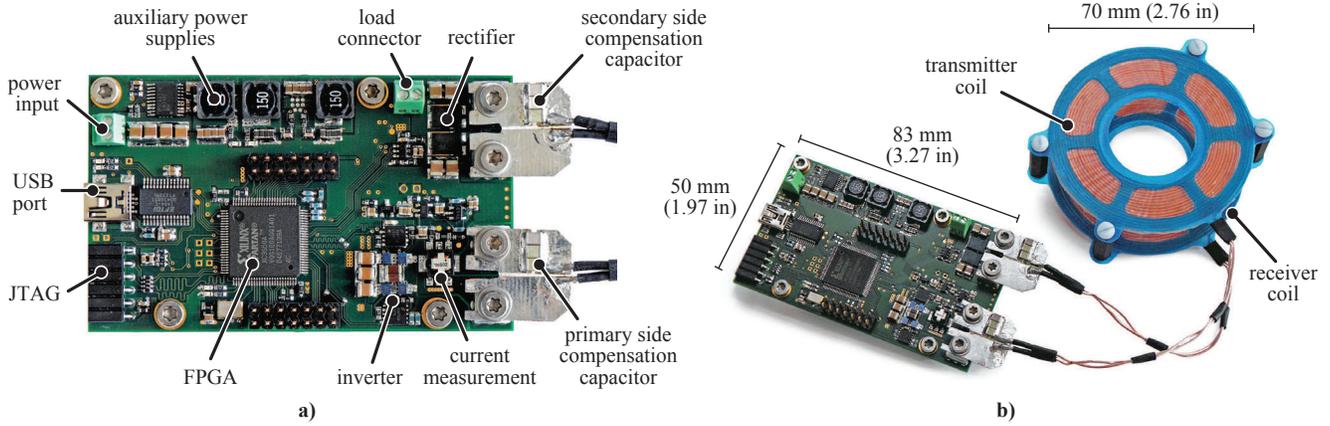
Figure 8: Photograph of the converter board and the TET system assembly including the prototype energy transmission coils.

The full-bridge inverter is based on the EPC2016 enhancement mode gallium nitride (eGaN) FET. The switches offer a very low on-resistance of $12\,\text{m}\Omega$ and a low output capacitance of $650\,\text{pF}$. Additionally the eGaN FETs feature a low total gate charge of $5\,\text{nC}$ and can be driven from $5\,\text{V}$ logic levels. This allows for a high switching frequency and lowers the gate driver losses considerably. Furthermore, the FET's outline dimensions are as small as 2.1 x 1.63 mm (0.083 x 0.064 in), which allows for a baord layout with ultra low inductance in the commutation path of each half-bridge, which increases the switching performance.

The secondary side full-wave rectifier is composed of Schottky barrier diodes with a low forward voltage drop of 0.38 V at a current of 1 A. For simplicity, the primary and secondary side circuit of the TET system are placed on the same printed circuit board (PCB). The compensation capacitors of the resonant circuit are mounted on separate PCBs, which can be connected to the test board using screw terminals, in order to simplify the testing of different coils at different operating frequencies. The gate signals for the inverter switches are generated with the aid of a Field Programmable Gate Array (FPGA) to achieve a high implementation flexibility. The FPGA is also intended to be used in future applications, including closed-loop control of the TET system output voltage.

B. Measurement Results

In order to verify the FE simulations and the analytical models, the measurements obtained with the prototype coils are compared to the simulated and calculated values. The results are shown in **Fig. 9 a)-c)**. The measured self inductance fit the simulated value with good agreement with a deviation of 4-7 %. The measured self-resonance frequencies of the primary and secondary side coils are 9.6 MHz and 12.2 MHz respectively, and are well above the operating frequency. **Fig. 9 b)** shows the measured, the calculated and the simulated values of the AC resistance and the resulting quality factor with respect to frequency. The calculated values fit the simulation with high accuracy. The measured AC resistance is approximately 14 % larger than the simulated value at 100 kHz. However, it was measured that the DC resistance of the used litz-wire was 11 % larger than the value specified in the manufacturer's datasheet. Taking this into account, the relative error of the measured value to the calculated AC resistance is 2.7 % at 100 kHz and 15 % at 1.5 MHz.

Table II: Component values and operating conditions of the prototype TET system.

a) Test Board Components	Value
Power FET T_1-T_4	EPC2016
Rectifier diodes D_1-D_4	V12P10-M3/87A
Capacitors C_1, C_2	2.97 nF / 1 kV
Capacitor C_f	40 µF / 50 V
b) Energy Transmission Coils	
Transmitter coil L_1	18.8 µH
Receiver coil L_2	18.4 µH
Litz wire	300 x 0.04 mm
Number of turns	16
Outside coil radius R_a	35 mm (1.38 in)
Inside coil radius R_i	17 mm (0.67 in)
c) Operating Conditions	
Switching frequency f_0	800 kHz
Output voltage U_{out}	35 V
Output power P_{out}	5 W - 30 W
Design coupling k_0	0.268
Max. coupling k_{max}	0.464

While the skin-effect losses can be neglected in comparison to the DC losses within the considered frequency range, the losses due to the proximity effect are increasing with frequency and are divided further into internal and external proximity losses as described in [15]. **Fig. 9 c)** shows the measured coupling factor at different coil separation distances, which is also in good agreement with the simulated values.

The prototype coils are operated with the specifications given in **Tab. II c)**. The output voltage of the TET system was set manually to a constant value of 35 V by adjusting the input voltage U_{in} of the inverter. The load was varied in a range of 5 to 30 W. All measurements were performed at the minimum and maximum coil separation distance of 10 mm and 20 mm, respectively. First, the phase angle of the input impedance, the voltage at the input and output as well as the currents in the resonant system were measured and are shown in **Fig. 9 d)-g)**. It can be seen in **d)** that the measured phase angle of the input impedance is in good agreement with the calculated
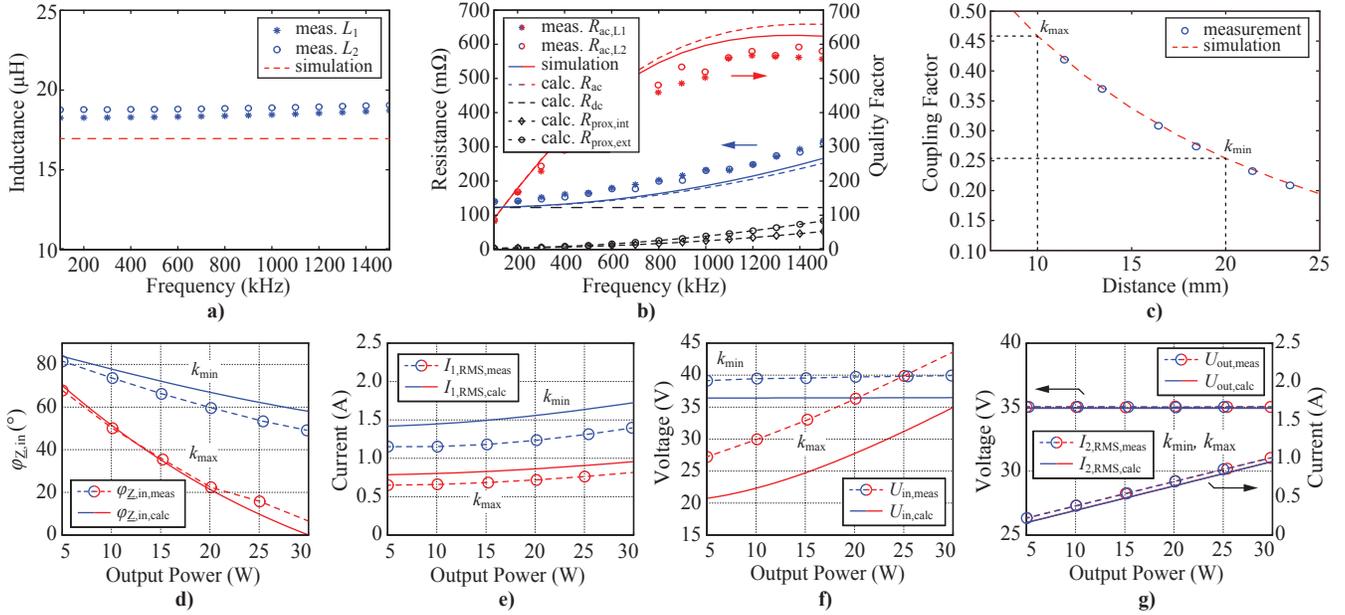
Figure 9: a)-c) Simulated, calculated and measured values of the self-inductance, the AC resistance and the coupling factor obtained with the prototype coils. The simulation is in good agreement with the measured data. However, the measured AC resistance at 100 kHz is about 14 % higher than the simulated and calculated value. As a reason it was found that the DC resistance of the used litz-wire is 11 % larger than the value specified in the manufacturers datasheet. **d)-g)** Measured and calculated phase angle of the input impedance and the input and output characteristics of the prototype system operated at the specified minimum and maximum coupling and at constant output voltage. The phase angle is in good agreement with the theoretical values. Deviations, specifically seen in the prediction of the input voltage in **f)** are due to the parasitic capacitances within the diode rectifier, which are not considered in the calculations.

values. However, the measured inverter input voltage and, thus, also the measured primary and secondary side RMS current values in **Fig. 9 e)** and **f)** show a constant deviation from the calculated values, specifically at maximum coupling. This discrepancy can be explained taking a closer look at the voltage and current waveforms within the rectifier circuit, shown in **Fig. 10**. Due to the large junction capacitance of 1.4 nF of the diodes at zero reverse voltage, the commutation of the diodes is delayed at the zero crossing of the secondary side current, because the junction capacitances must be either charged or discharged by the secondary side current i_2 in order to commutate the current to the active branch of the rectifier circuit. During this time interval, there is no energy supplied to the output, which results in the deviation from the predicted voltage gain. In addition, due to the resulting phase-shift between the secondary side current i_2 and the fundamental of the rectifier input voltage u_2, the assumption of the purely resistive equivalent load model given in (4) is not valid any more. In the following, it will be shown that the rectifier diodes must be replaced by a synchronous rectifier using active switches, which will eliminate the explained issue, as long as the output capacitances of the switches are considerably small compared to the junction capacitance of the Schottky diodes.

Second, in order to calculate the efficiency, the input and output power of the prototype TET system was measured for an output power range of 5 to 30 W. The input power includes the power delivered to the inverter power stage and the power consumed by the gate drives. The constant power losses of 258 mW caused by the FPGA and the auxiliary circuits are not included in the efficiency calculation. The results of the power loss measurement and the
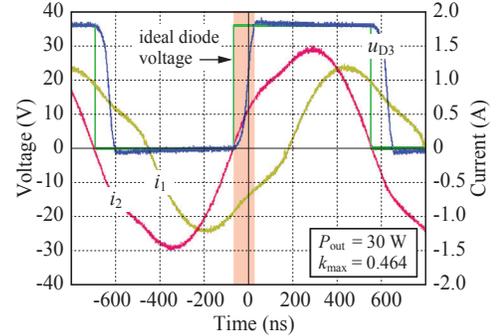
Figure 10: Deviation of the measured rectifier diode u_{D3} from the ideal switching waveform, as well as the primary and secondary side currents i_1 and i_2. The red shading highlights the time interval, where the parasitic capacitances of the rectifier diodes must be either charged or discharged in order to commutate the current to the active branch of the rectifier.

efficiency are shown in **Fig. 12 a)** and **b)** as a function of the output power. It can be seen that even at the minimum coupling factor, an efficiency of well over 90 % was achieved at the maximum output power. The calculations of the power loss and the efficiency fit the measured values with good accuracy, specifically at low coupling and light loading conditions, where the phase angle of the input impedance is large and soft-switching is achieved. This operation condition corresponds to point 1) in **Fig. 12 b)**.

The prototype system was designed for a zero phase angle of the input impedance at the maximum coupling and the maximum output power. However, as it was explained in **Section III**, it is important to choose the design coupling k_0 such that the impedance seen by
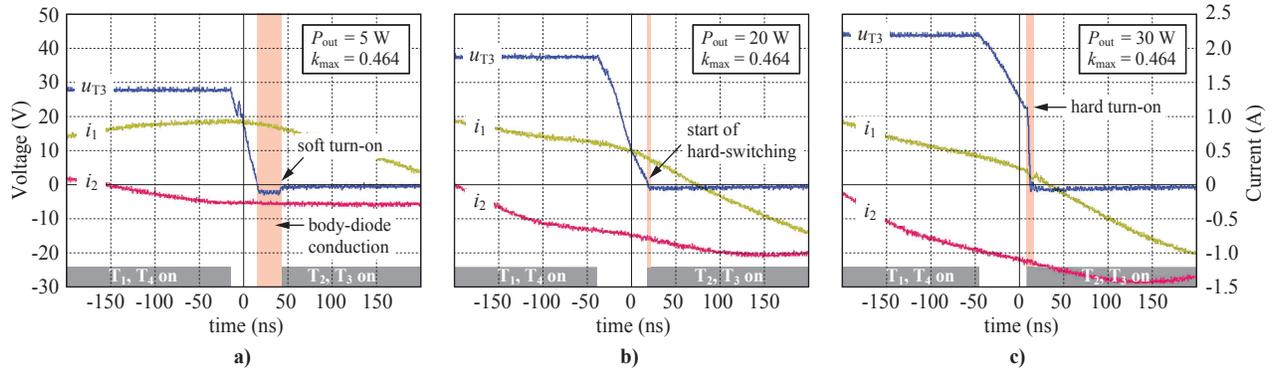
Figure 11: Measured switching transition of the FET voltage u_{T3} and the primary and secondary side currents i_1 and i_2 for the operating points denoted by 1)-3) in **Fig. 12**. In **a)**, the input impedance of the resonant system is highly inductive and soft switching of the switches is achieved. **b)** Point of operation, where the current i_1 is just sufficient to discharge the output capacitances of the switches T_2 and T_3 before they are turned on. In **c)**, the phase angle of the input impedance of the resonant system is too small for the current i_1 to discharge the output capacitance of T_2 and T_3 completely and the result is a hard turn-on of the corresponding switches.
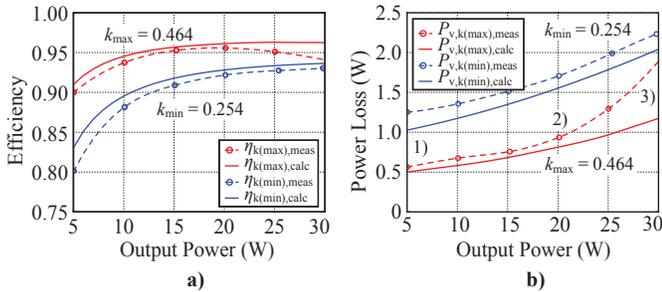
Figure 12: a) Measured and calculated efficiency of the prototype system, operated at maximum and minimum coupling under variable loading. **b)** Total power losses, excluding the power consumed by the auxiliary power supplies and the control circuit. 1)-3) denote the operating points corresponding to the switching waveforms of the inverter shown in **Fig. 11 a)-c)**. The calculations do not account for switching losses, which explains the deviation from the measured values at point 3).

Figure 13: Calculated power loss distribution within the TET system at the minimum and maximum coil separation distance and maximum output power.

the inverter is still inductive and that the inverter's output current is large enough to achieve ZVS. As the phase angle of the input impedance decreases, soft switching is lost and the inverter losses are increasing, which corresponds to the point 2) and 3) in **Fig. 12 b)**. The loss calculation does not account for switching loss, which explains the deviation of the measurement to the estimated values at maximum coupling and high output power. The voltage and current waveforms at the operating points 1)-3) in **Fig. 12 b)** are shown in **Fig. 11 a)-c)** respectively. In **a)** the input impedance seen by the inverter is highly inductive and the inverter's output current is large enough to charge and discharge the output capacitances of the switches well before the end of the dead-time interval and the switches T_2 and T_3 can turn on at zero voltage. The red shading highlights the reverse conduction time interval of the switches T_2 and T_3. The eGaN FETs exhibit a source-drain forward voltage drop of approximately 1.5 V at 1 A, which is much higher than the voltage drop of the body diode of a silicon MOSFET. Therefore, during this time interval, a considerable amount of energy is dissipated within the switches. The losses associated with the reverse conduction could be reduced by a dynamical adjustment of the dead-time interval or by placing a Schottky diode anti-parallel to the switch [18]. The

small package of the FET allows for the low commutation inductance needed for a fast commutation of the current from FET to the parallel Schottky diode. Furthermore, the high reverse conduction voltage drop helps to reduces the commutation time additionally. **Fig. 11 b)** shows the point of operation, where the output current of the inverter is just large enough to discharge the output capacitances of the switches T_2 and T_3, before they are turned on. Increasing the output power from this point of operation results in a further reduction of the phase angle of the resonant circuit's input impedance and the inverter switches experience hard switching. This point of operation is shown in **Fig. 11 c)** and corresponds to the point 3) in **Fig. 12 b)**. The primary current i_1 is too small to completely discharge the output capacitances of the switches T_2 and T_3 (and charge the capacitances of T_1 and T_4). As a result, the remaining stored energy will be dissipated during turn-on.

To identify the starting point for further improvements, the distribution of the losses within the prototype system are calculated

at the minimum and maximum coupling. The results are shown in **Fig. 13 a)** and **b)**. The secondary side coil losses are very low and contribute only 8-9 % to the total losses. The losses associated with the diode rectifier account for 81.5 % of the total secondary side losses at both operating points. The small size of the rectifier together with the high amount of losses will make it difficult to keep the heating of the tissue within save limits. Therefore, the future work will include the development of a synchronous rectification which has the potential to significantly reduce the losses in the rectifier circuit.

On the primary side, the losses within the inverter circuit make the largest contribution. In the operating point corresponding to **Fig. 13 a)**, the input impedance of the resonant circuit is highly inductive and the primary side current is larger than the secondary side current due to the increased reactive power flowing in the primary resonant circuit. Soft-switching can be achieved at any time, but, as it was shown previously, reverse conduction losses are generated during the dead-time. **Fig. 13 b)** shows the operating conditions corresponding to **Fig. 11 c)**, where soft-switching is not achieved. In this situation, the switching losses make up almost 70 % of the total primary side losses. This shows clearly, that a purely resistive operation of the IPT system is not practical and a minimum positive phase angle of the input impedance of the resonant circuit is needed at the highest coupling and maximum power, in order to ensure that the inverter's output current is large enough to allow for zero voltage switching.

VI. Conclusions & Future Work

In this paper, the optimization process of an effective energy transmission system for high power medical applications is described with the focus on the minimization of the power losses associated with the implanted receiver coil. The characteristics of the considered TET system was studied in detail and meaningful design equations are presented for the series-series compensated system. Additionally, the design for optimal load-matching is shown and the graphical representation in the load-matching plane is explained. The optimization showed that with the use of a high TET system output voltage and a high operating frequency, it is possible to use coils with higher *FOM*, while maintaining load matching at the operating point with load independent voltage gain. It was also shown, that for a series-series compensated system, load independent voltage gain and optimal matching at maximum load can be achieved at a fixed coupling and operating frequency at the same time. From the thermal simulations it was found, that depending on the coil diameter, a power loss of up to 500 mW can be tolerated within the receiver coil while keeping the temperature within save limit. The prototype TET system shows a high efficiency well above 90 % at full power and the measurements validate the theoretical results with good accuracy. The loss calculation and the measurements have shown, that the rectifier make the largest contribution to the secondary side losses and will be replaced by a synchronous rectifier in the future work. Additionally, the battery charging controller will be designed and optimized for lowest volume and losses.

References

[1] M. S. Slaughter and T. J. Myers, "Transcutaneous energy transmission for mechanical circulatory support systems: history, current status, and future prospects," *J. Card. Surg.*, vol. 25, no. 4, pp. 484–489, 2010.

[2] J. C. Schuder, "Powering an artificial heart: birth of the inductively coupled-radio frequency system in 1960," *Artificial Organs*, vol. 26, no. 11, pp. 909–915, 2002.

[3] W. L. Holman, S. V. Pamboukian, D. C. McGiffin, J. A. Tallaj, M. Cadeiras, and J. K. Kirklin, "Device related infections: are we making progress?" *J. Card. Surg.*, vol. 25, no. 4, pp. 478–483, 2010.

[4] A. El-Banayosy, L. Arusoglu, L. Kizner, M. Morshuis, G. Tenderich, E. Pae, W, and R. Körfer, "Preliminary experience with the LionHeart left ventricular assist device in patients with end-stage heart failure," *Ann. Thorac. Surg.*, vol. 75, no. 5, pp. 1469–1475, 2003.

[5] Greatbatch Medical (May 2014), "Xcellion rechargeable batteries." [Online]. Available: http://www.greatbatchmedical.com/assets/products/Xcellion Rechargeable Batteries.pdf

[6] C.-S. Wang, G. A. Covic, and O. H. Stielau, "Power transfer capability and bifurcation phenomena of loosely coupled inductive power transfer systems," *IEEE Trans. Ind. Electron.*, vol. 51, no. 1, pp. 148–157, 2004.

[7] W. Zhang, S.-C. Wong, C. K. Tse, and Q. Chen, "Analysis and comparison of secondary series- and parallel-compensated inductive power transfer systems operating for optimal efficiency and load-independent voltage-transfer ratio," *IEEE Trans. Power Electron.*, vol. 29, no. 6, pp. 2979–2990, 2014.

[8] Q. Chen, S.-C. Wong, C. K. Tse, and X. Ruan, "Analysis, design, and control of a transcutaneous power regulator for artificial hearts," *IEEE Trans. Biomed. Circuits Syst.*, vol. 3, no. 1, pp. 1932–4545, 2009.

[9] I. Nam, R. Dougal, and E. Santi, "Optimal design method to achieve both good robustness and efficiency in loosely-coupled wireless charging system employing series-parallel resonant tank with asymmetrical magnetic coupler," *Proc. IEEE Energy Convers. Congr. and Expo. (ECCE USA)*, pp. 3266–3276, 2013.

[10] I. Nam, R. Dougal, and E. Santi, "Optimal design method for series LCLC resonant converter based on analytical solutions for voltage gain resonant peaks," *Proc. IEEE Appl. Power Electron. Conf. and Expo. (APEC)*, pp. 1429–1437, 2013.

[11] K. V. Schuylenbergh, *Inductive Powering: Basic Theory and Application to Biomedical Systems*, 1st ed. Springer Science, 2009.

[12] E. Waffenschmidt and T. Staring, "Limitation of inductive power transfer for consumer applications," in *Proc. European Conf. on Power Electron. and Appl. (EPE)*, 2009, pp. 1–10.

[13] R. Bosshard, J. W. Kolar, J. Mühlethaler, I. Stevanović, B. Wunsch, and F. Canales, "Modeling and η-α-Pareto optimization of inductive power transfer coils for electric vehicles," *IEEE J. Emerg. Sel. Topics Power Electron.*, 2014, (accepted for publication).

[14] R. L. Steigerwald, "A comparison of half-bridge resonant converter topologies," *IEEE Trans. Power Electron.*, vol. 3, no. 2, pp. 174–182, 1988.

[15] J. Mühlethaler, "Modeling and multi-objective optimization of inductive power components," Ph.D. dissertation, Swiss Federal Institute of Technology Zurich (ETHZ), 2012.

[16] The IT'IS Foundation Website (Feb. 2014), "Database of tissue properties." [Online]. Available: http://www.itis.ethz.ch/itis-for-health/tissue-properties/database/

[17] T. R. Gowrishankar, D. A. Stewart, G. T. Martin, and J. C. Weaver, "Transport lattice models of heat transport in skin with spatially heterogeneous, temperature-dependent perfusion," *BioMedical Engineering OnLine*, vol. 3, no. 42, 2004.

[18] EPC - Efficient Power Conversion (June 2014), "Dead-time optimization for maximum efficiency." [Online]. Available: http://epc-co.com/epc/documents/papers/Dead-Time Optimization for Maximum Efficiency.pdf